



HAL
open science

Multipactor predictions for ion cyclotron resonance heating antennas of the tokamak WEST

Eva Al Hajj Sleiman, Julien Hillairet, Mohamed Belhaj, Sarah Dadouch,
Vincent Maquet

► **To cite this version:**

Eva Al Hajj Sleiman, Julien Hillairet, Mohamed Belhaj, Sarah Dadouch, Vincent Maquet. Multipactor predictions for ion cyclotron resonance heating antennas of the tokamak WEST. Nuclear Fusion, 2023, 63 (12), pp.126054. 10.1088/1741-4326/ad0509 . hal-04277422

HAL Id: hal-04277422

<https://hal.science/hal-04277422>

Submitted on 9 Nov 2023





HAL is a multi-disciplinary open access archive for the deposit and dissemination of scientific research documents, whether they are published or not. The documents may come from teaching and research institutions in France or abroad, or from public or private research centers.

L'archive ouverte pluridisciplinaire **HAL**, est destinée au dépôt et à la diffusion de documents scientifiques de niveau recherche, publiés ou non, émanant des établissements d'enseignement et de recherche français ou étrangers, des laboratoires publics ou privés.



Distributed under a Creative Commons Attribution 4.0 International License

Multipactor predictions for ion cyclotron resonance heating antennas of the tokamak WEST*

Eva Al Hajj Sleiman^{1,2,**} , Julien Hillairet¹ , Mohamed Belhaj² , Sarah Dadouch² and Vincent Maquet³ 

¹ CEA, IRFM, 13108 Saint Paul Les Durance, France

² ONERA, DPHY, Université de Toulouse, 31055 Toulouse, France

³ Laboratory for Plasma Physics, LPP-ERM/KMS, 1000 Brussels, Belgium

E-mail: eva.alhajjsleiman@cea.fr

Received 31 July 2023, revised 2 October 2023

Accepted for publication 19 October 2023

Published 6 November 2023



Abstract

During the plasma experimental campaigns performed on the tokamak WEST, a performance-limiting observation has been made on the Ion Cyclotron Resonance Heating (ICRH) system composed of three identical antennas. When only one antenna is powered while the remaining two are off, an increase in the internal pressure is measured within the non-powered antennas. The internal pressure of the non-powered antennas exceeds a safety pressure interlock whose threshold is 4.5×10^{-3} Pa, and consequently, the application of the RF power is prohibited to avoid plasma creation within these antennas. In this paper, the multipactor phenomenon caused by the inter-antennas' coupling is shown to be responsible for the pressure increase observed in the non-powered antennas. Additionally, an analytic estimation of the pressure rise caused by the multipactor is compared to that observed experimentally.

Keywords: multipactor, WEST, ICRH, plasma, pressure, coupling

(Some figures may appear in colour only in the online journal)

* We would like to thank Jean-François Roussel for the help provided to understand the physical aspect of the particles' desorption problem. This work has been carried out within the framework of the EUROfusion Consortium, funded by the European Union via the Euratom Research and Training Programme (Grant Agreement No. 101052200—EUROfusion). Views and opinions expressed are however those of the author(s) only and do not necessarily reflect those of the European Union or the European Commission. Neither the European Union nor the European Commission can be held responsible for them.

** Author to whom any correspondence should be addressed.



Original Content from this work may be used under the terms of the [Creative Commons Attribution 4.0 licence](https://creativecommons.org/licenses/by/4.0/). Any further distribution of this work must maintain attribution to the author(s) and the title of the work, journal citation and DOI.

All rights reserved

1. Introduction

Ion Cyclotron Resonance Heating (ICRH) is an auxiliary heating system commonly employed on nuclear fusion devices such as tokamaks. ICRH system is a bulk plasma heating method based on the resonance principle between the cyclotron motion of an ion in a static magnetic field and the plasma wave having the same frequency.

On the tokamak WEST, located in Cadarache, France, two Radio-Frequency (RF) heating systems are available [1]: (i) the ICRH system composed of three identical antennas operating in the frequency range [46–65] MHz during continuous wave operation [2], and (ii) two Lower Hybrid Current-Drive (LHCD) antennas operating at 3.7 GHz [3]. An illustration of the vacuum vessel of the tokamak WEST, along with the locations of the different heating systems, is given in figure 1. We are mainly interested in the ICRH system to address a problem limiting the operation of the antenna system.

Although the three WEST ICRH antennas are operated at slightly different frequencies, cross-talk between antennas is evidenced, as shown herein. During the experimental campaigns on WEST, the following observation has been made on all three ICRH antennas during plasma operations: if one ICRH antenna is powered with the remaining antennas being off, a pressure rise (from $\sim 10^{-5}$ Pa to a pressure ranging between 10^{-3} Pa – 10^{-2} Pa) is observed in the non-powered antennas. If the pressure exceeds the predefined safety threshold $p_{th} = 4.5 \times 10^{-3}$ Pa [4], a safety interlock prohibits the (re-)application of the RF power to avoid generating and sustaining an RF-induced plasma inside the antennas, which can affect the operation of the ICRH system, for example by preventing the use of another antenna later in the plasma scenario. Therefore, this phenomenon can complicate or even stop the antennas' nominal operations. A pressure rise example is shown in figure 2, where a single ICRH antenna is operated (Q_1), and the remaining two are off (Q_2 and Q_4). When the antenna Q_1 couples its power to the plasma, the pressure increases inside the two powered-off antennas (Q_2 and Q_4). This pressure is sufficient to prohibit Q_2 and Q_4 's use, as it is above the predefined security threshold p_{th} .

One possible cause explaining these observations is the multipactor phenomenon [5], a resonant RF vacuum discharge induced by antenna cross-talking. A possible worst-case consequence is the metallization of the capacitors' ceramics or the RF feed-through window if multipactor-induced plasma is sustained in its vicinity.

A similar observation has also been made on the ICRH system of the Alcator C-Mod tokamak [6, 7]. The authors' work identified the multipactor-induced glow discharge as the principal cause of neutral pressure limitations observed on Alcator C-Mod, constraining its operation. Indeed, the development of the gas breakdown is affected by the electron population's increase and the gas density increase by molecules' desorption from the surfaces. The latter increases the rate of gas ionization by electron impact.

The paper aims to validate whether the multipactor explains the pressure rise occurrence during plasma operations by dividing the analysis into two main steps. In the first step,

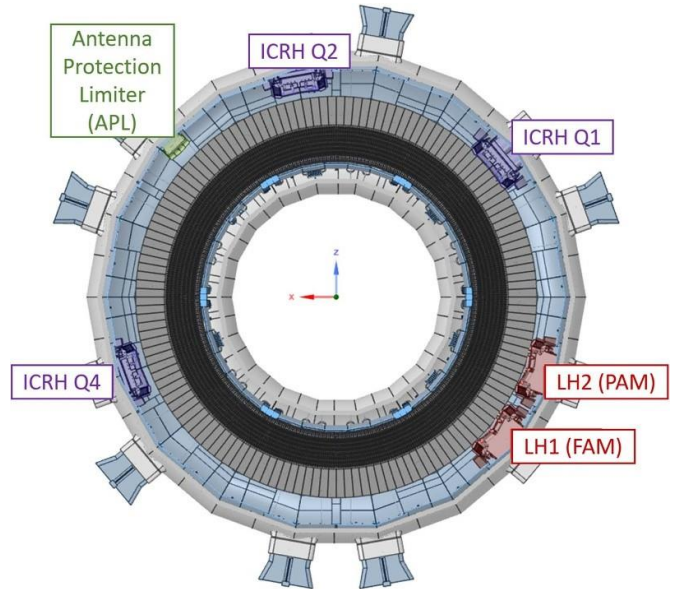


Figure 1. A top view illustration of the vacuum vessel of the tokamak WEST, with the different RF heating systems' employment: in purple three ion cyclotron resonance heating (ICRH) antennas, in red two lower hybrid current drive (LHCD) antennas, and in green the moveable antenna protection limiter.

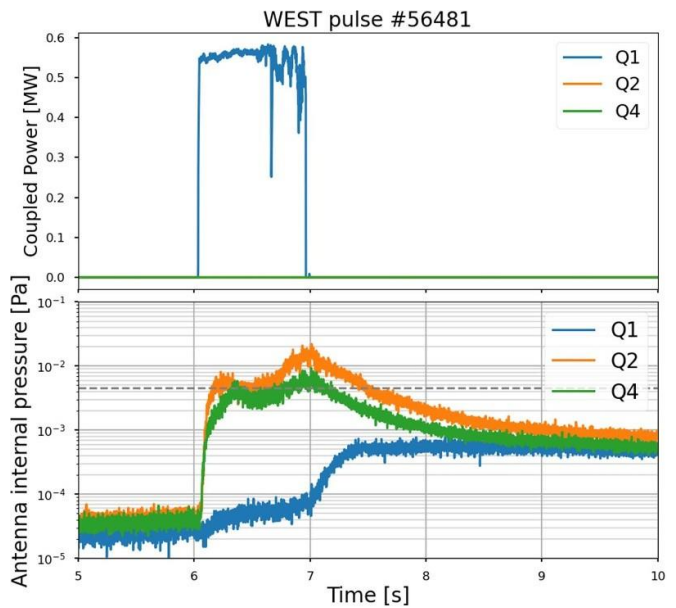


Figure 2. An example demonstrating the pressure rise in the off-mode antennas (Q_2 and Q_4) on plasma when only one antenna is on (Q_1 , operating with 0.55 MW). The antennas' coupled powers are plotted in the top figure versus time. In the bottom figure, the antennas' internal pressure is plotted versus time, and the dashed grey line represents the pressure rise limit (p_{th}) beyond which the (re-)application of RF power is prohibited for security reasons.

we determine the generator's forward power range triggering the multipactor phenomenon in the various components of the ICRH system during plasma operations. The latter characterizes the multipactor occurrence in the non-powered ICRH antennas when only one antenna is powered. Yet, the second

step is crucial for determining the pressure rise level caused by the multipactor phenomenon to compare it to the pressure rise level observed experimentally.

The rest of the paper is organized as follows: section 2 recalls the definition of the multipactor phenomenon and its consequences on the heating system of a tokamak. Section 3 describes the WEST ICRH antenna and highlights the methodology used to address the multipactor occurrence in its various components. Section 4 presents the multipactor triggering forward powers when only one ICRH antenna is active in a plasma scenario. Section 5 formulates the pressure rise problem to estimate the pressure increase level caused by the multipactor phenomenon and compare it to the experimental pressure rise. Section 6 concludes the work.

2 Multipactor phenomenon

Multipactor is a vacuum discharge observed in microwave structures at sufficiently low pressures when the electron mean free path becomes longer than the electrodes' separation distance [5]. The multipactor mechanism sustains itself by the secondary electron emission resulting from electrons' impact on the RF device's surfaces with sufficient kinetic energy to release, on average, more secondary electrons than the number of impinging electrons—so that more electrons are generated than removed. The secondary electron emission could come either from a metallic or dielectric surface. Two conditions, found in [5, 8–11], must be simultaneously fulfilled to trigger the multipactor.

For nuclear fusion devices, multipactor affects or limits the heating antennas' performance, reduces the reliability of the RF heating and current-drive systems, and limits the maximum power coupled to the plasma [12, 13]. Furthermore, the multipactor can induce a gas breakdown at lower gas pressures than expected by a regular *RF Paschen* breakdown, especially in the case of high DC magnetic fields [6, 7]. In addition, multipactor electrons' clouds can induce reflected power (detuning) to the antennas and eventually damage the high-power sources. If not stopped, the temperature rise, and the subsequent increase of pressure due to particles' desorption, caused by multipactor, can lead to RF components' damage, such as the vacuum feed-through ceramics by excess heat stress or its metallization by arc-induced sputtering [14] up to causing a puncture or a fracture that can lead to a vacuum break event. Subsequently, a sustained multipactor event can trigger a corona discharge leading to components' partial or total destruction [15, 16]. Indeed, some damaging gas discharges are initiated by the increased outgassing triggered by the multipactor and the local pressure rise [17].

3 Multipactor in WEST ICRH antennas

3.1 WEST ICRH antennas' description

The WEST ICRH system is made of three identical antennas. Each antenna, represented in figure 3, is fed by two

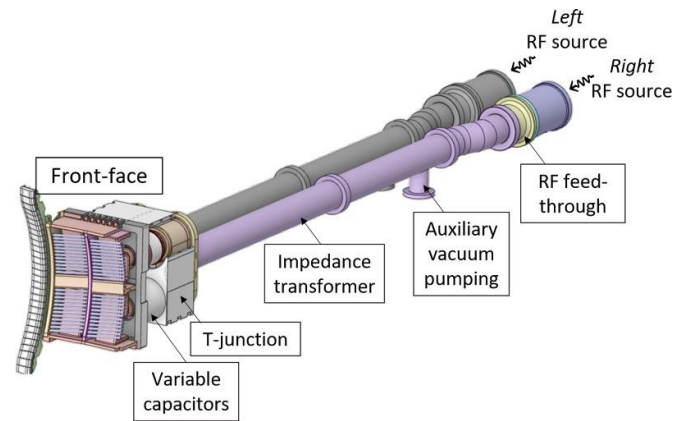


Figure 3. An illustration of the different components of one ICRH antenna used on the tokamak WEST. Each side has its own high-power generator.

generators—one generator per antenna side. On plasma operation, the power delivered by each generator ranges from 100 kW up to 1.5 MW. The electromagnetic power is transported by feeding 30 Ω coaxial transmission lines. From the generators' side, following the nitrogen-pressurized transmission lines is the sealing RF feed-through barrier—coaxial feed-through made of a cylindrical ceramic piece—ensuring the tightness between the nitrogen-pressurized transmission lines and the under-vacuum components.

Under vacuum conditions, following the RF feed-through is the matching system composed of a two-stage matching network. The first stage is a passive two-stage quarter-wavelength impedance transformer [4, 18]. The second stage is a tuneable internal conjugate-T [19], composed of tuneable capacitors connected in parallel via a T-junction (referred to as 'bridge').

The impedance transformer is designed to match the impedance of the RF feed-through window to the input port's impedance of the T-junction on a broad range of frequencies. It is made of two quarter-wave stages, where the first stage is connected to the RF feed-through and is of 17.4 Ω characteristic impedance, and the second stage of 5.5 Ω characteristic impedance and is connected to the T-junction's input port.

The rears of the two impedance transformers of each ICRH antenna are connected to one vacuum auxiliary pumping system, which aims to improve the vacuum conditions inside the antenna. Each impedance transformer of one antenna side is equipped with a pressure gauge (so two pressure gauges per ICRH antenna) for pressure monitoring during operation. The auxiliary pumping system location is shown in figure 3.

The second stage of the matching system consists of a T-junction with the input port connected to the impedance transformer and the two output ports, each connected to a matching—tuneable—capacitor.

Each WEST ICRH antenna's front face—connecting the antenna sides—is a phased array of loop radiators, denoted *straps*. Therefore, each WEST ICRH antenna is a four-straps antenna (2 poloidal \times 2 toroidal), composed of two toroidal sides that we will refer to as *left* and *right* sides (as seen

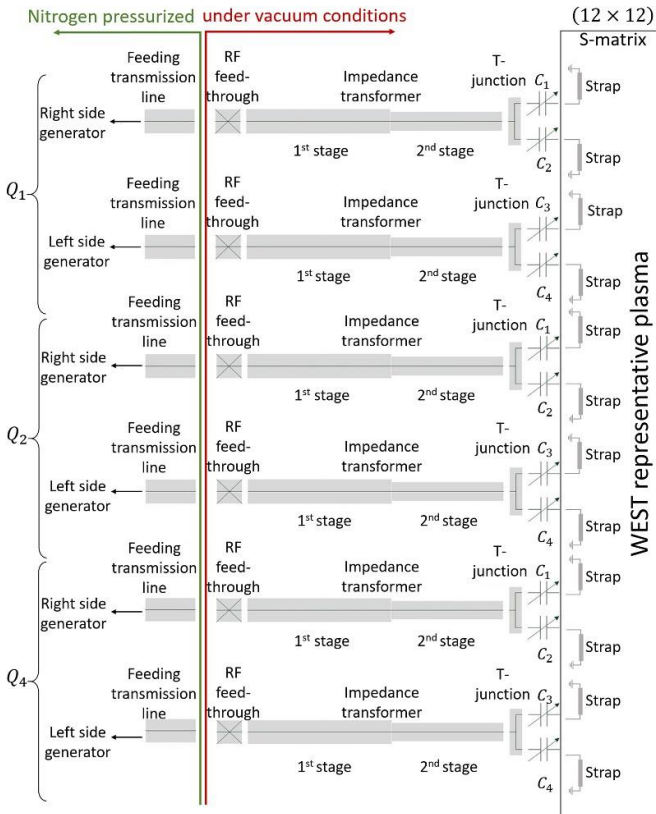


Figure 4. Circuit model of the three WEST ICRH antennas facing a plasma, where both sides of each antenna are modelled. The WEST representative plasma scenario is represented by a (12×12) S-matrix to take into account the RF coupling between the ICRH antennas. Each simplified circuitual schematic represents one WEST ICRH antenna and is constituted of two sides. Each side is constituted of a radio-frequency generator, feeding transmission lines, RF feed-through, matching system—T-junction, impedance transformer, and two capacitors. The two sides are connected to the antenna front face composed of four straps.

from the exterior of the torus), each fed by a high power source, and constituted of one RF feed-through, one impedance transformer, one T-junction, and two parallel tuneable capacitors.

The circuitual representation of each WEST ICRH antenna is given in figure 4.

3.2 Methodology description

We want to investigate if the multipactor is responsible for the pressure rise measured in the non-powered ICRH antennas when only one antenna is powered. The latter is achieved by determining the generator's forward power range, triggering the multipactor within the off-mode antennas during plasma operations. In such scenarios, the antennas facing plasma have a high coupling which depends on the plasma properties, where an important fraction (up to 1.5 MW [2]) of the generators' power is coupled to the plasma but also to the other antennas.

During the WEST ICRH antennas' operation, the operator has to make the following decisions:

- choosing the number of active antennas and its (their) forward power(s);
- choosing the frequency at which the two generators feed an antenna;
- tuning the capacitors of the antenna(s) at its (their) frequency(ies) of interest. Two main situations are found: (i) the capacitors are tuned to match the frequency of the generators and are called *tuned capacitors*. (ii) The capacitance of each capacitor is set to 120 pF—highest capacitance value, and are called *detuned capacitors*, as the antenna is no more resonant.

During plasma operations, when an antenna is powered, both sides are equally powered, generally in dipole configuration—with a 180° phase difference between both sides—and the four capacitors of the antenna are tuned to make it resonant at the frequency of interest.

Therefore, our goal is twofold: (i) determine the generators' forward powers and capacitor states that can trigger multipactor inside the different sides and components of the antennas at the frequency of interest, and (ii) suggest—if there are any—the best strategies to reduce or avoid multipactor in plasma operational scenarios. To achieve our goals, we have developed a methodology detailed in [11], which was applied to study the multipactor occurrence during the RF conditioning phase—under vacuum (no plasma)—of each WEST ICRH antenna.

We summarize herein the methodology's main steps [11]:

- Determine the *multipactor electric field thresholds* for the various components constituting the WEST ICRH antennas while accounting for the standing wave patterns: T-junction and the impedance transformer while taking two ICRH extreme relevant electron emission properties of the components' stainless steel silver-coated material: *non-conditioned* Total Electron Emission Yield (TEEY) mimicking the material properties before the RF conditioning phase—worst case scenario, and *fully-conditioned* TEEY to mimic the material properties at the end of the RF conditioning phase—best case scenario. The TEEY of both cases are illustrated in figure 5. These two structures were analyzed in detail in [11].

Furthermore, to complete the multipactor analysis, using Ansys-HFSS⁴, we have simulated the *multipactor electric field thresholds* for RF feed-through, which is a multi-material structure, illustrated in figure 6. Following the procedure analysis of [11], the RF feed-through is split into two regions: a conical silver-coated transmission line region (*Pre-Window*) and a multi-material region composed of a silver-coated conductor and the

⁴ Version 2023 R2.

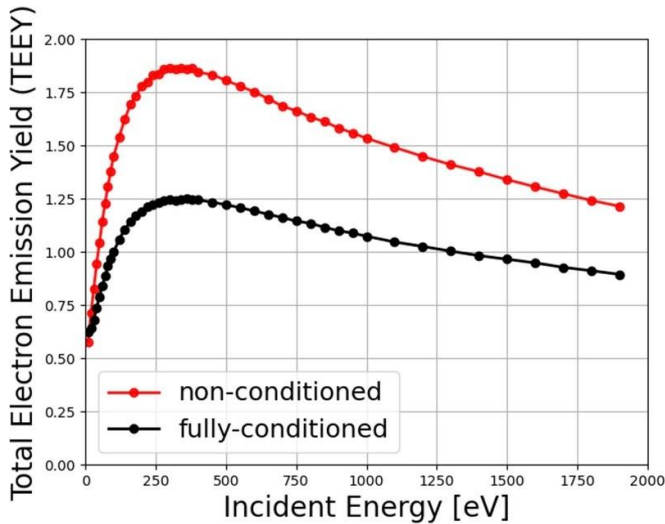


Figure 5. TEEY measurements for a WEST ICRH representative silver-coated sample baked for three days and maintained at 70 °C [10, 11]. In red, the TEEY data are measured before any conditioning treatment; and in black, the TEEY data are measured after a full conditioning treatment (with a cumulative electron dose of 2338 μCmm^{-2}).

alumina ceramic (*Window*). The analysis has shown that the *Pre-Window* region is not prone to multipactor for the *non-conditioned* and the *fully-conditioned* TEEY data curves of a silver-coated stainless steel representative sample of the ICRH antenna (red and black curves of figure 5). Whereas, the *Window* region is prone to multipactor when the *non-conditioned* TEEY curve of silver (red curve of figure 5) and the *as-received* TEEY data curve of alumina (blue curve of figure 7) are assigned. Nevertheless, the *fully-conditioned* TEEY curve of silver (black plot of figure 5) and the *conditioned* TEEY data curve of alumina (orange plot of figure 7) show no multipactor occurrence in the structure.

It should be noted that the multipactor thresholds are determined without accounting for the toroidal DC magnetic field of the WEST torus.

- (b) Solving for the electric field in the antenna sections, using a full-wave and a circuit solver (ANSYS Electronics) to determine the *excited electric fields*.
- (c) Comparing the *multipactor electric fields thresholds* to *excited electric fields*, to determine the forward generators' powers—lower and upper thresholds—triggering multipactor inside the various components of the antennas.

3.3 Plasma's test-cases

While ICRH operators define the generator frequencies and the four matching capacitance values for all three ICRH antennas, the WEST plasma control system sets the RF power of the generators, feeding both sides. We will study the following two operational cases:

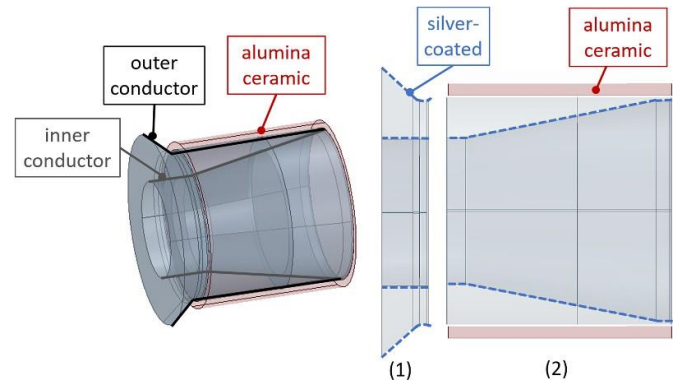


Figure 6. Left—the design of the RF feed-through, where in red the alumina ceramic is represented, in grey the inner conductor, and in black the outer conductor. Right—the cut view representation of each of the RF feed-through multipactor regions. The RF feed-through is divided into two different multipactor regions: (1) — *Pre-Window* of silver-coated stainless steel material, (2) — *Window* of multi-material structure (alumina and silver-coated stainless steel).

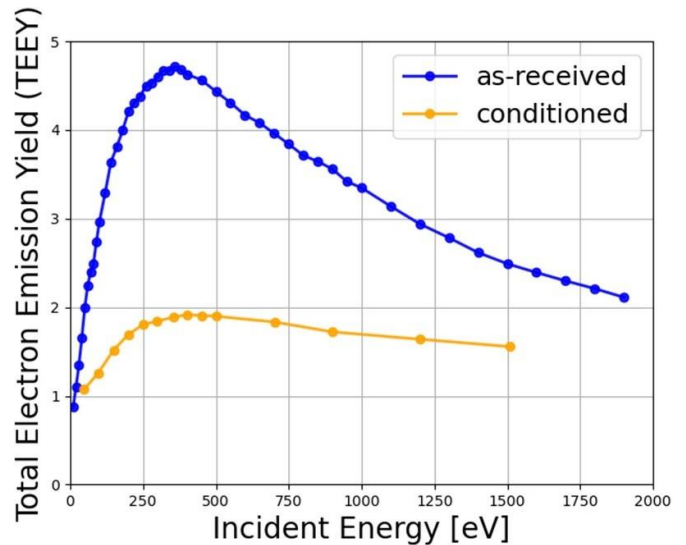


Figure 7. In blue, the TEEY data for an as-received alumina sample (measured at ONERA/DPHY). In orange, the TEEY data for a conditioned alumina sample. The conditioned TEEY data are extracted from [20].

Case 1: One ICRH antenna is on—the generators of both sides are powered—and the four capacitors are *tuned* at 55 MHz. The antenna is operated in dipole—with a 180° phase difference between both sides. The remaining two antennas are off, and their capacitors are *tuned* at 55 MHz.

Case 2: One ICRH antenna is on—the generators of both sides are powered—and the four capacitors are *tuned* at 55 MHz. The antenna is operated in dipole—with a 180° phase difference between both sides. The remaining two antennas are off, and their capacitors are *detuned*.

The circuit model of three ICRH antennas during plasma scenarios is represented in figure 4, where each antenna side's

components are modeled. In particular, all the components (RF feed-through, T-junction, and impedance transformer) of the *left* and *right* sides of each antenna are taken into consideration using their full-wave models in ANSYS Circuit, except for the capacitors that are modeled using an equivalent lumped circuit determined from a fitting of a full-wave model [21]. Moreover, an S-matrix representative of a WEST plasma scenario is obtained by a full wave model of the WEST torus with the three ICRH front faces. Therefore, this matrix has a (12×12) dimension as each antenna front face is a four ports passive component.

Solving self-consistently the simulation leads to the *excited electric fields*'s determination in all the components of the three WEST ICRH antennas, which is then used to deduce the multipactor occurrence in each region of interest of each structure of the three antennas [11].

4. Results—multipactor-triggering generators' forward powers

In this section, we determine for each component of each antenna side the lower and upper one side generator forward powers triggering the multipactor at the frequency of 55 MHz.

4.1 Results-case 1

In this first case, both generators of the antenna Q_1 are powered with the same forward power, and the four capacitors are *tuned* for the antenna to resonate at 55 MHz. Q_2 and Q_4 are non-powered with their capacitors *tuned* at 55 MHz.

First, we have considered the *non-conditioned* TEEY data curve (red curve of figure 5) for the silver-coated components and the as-received TEEY data curve for the alumina ceramic (blue curve of figure 7). The results are illustrated in figure 8 where we have represented the range of the forward generator's power—the forward power range corresponding to the generator of one side of the powered antenna—triggering the multipactor in each antenna component: T-junction, impedance transformer and the RF feed-through. The blue (respectively black) vertical lines correspond to the forward powers triggering multipactor within the RF components of the *left* (respectively *right*) side of each antenna. The grey hatched region corresponds to the operational nominal power range of one powered generator [100 kW–1.5 MW].

It could be remarked that within the operational range of one generator of the WEST ICRH antennas, the multipactor is triggered in all the components of the non-powered antennas (Q_2 and Q_4) except for the T-junction and RF feed-through of the *left* side of the Q_2 antenna as the electric field observed in their multipactor regions, within the [100 kW–1.5 MW] power range, is not enough for the multipactor to be triggered in these components. The latter could be attributed to the anisotropic characteristics of the non-symmetrical S-matrix of the simulated plasma.

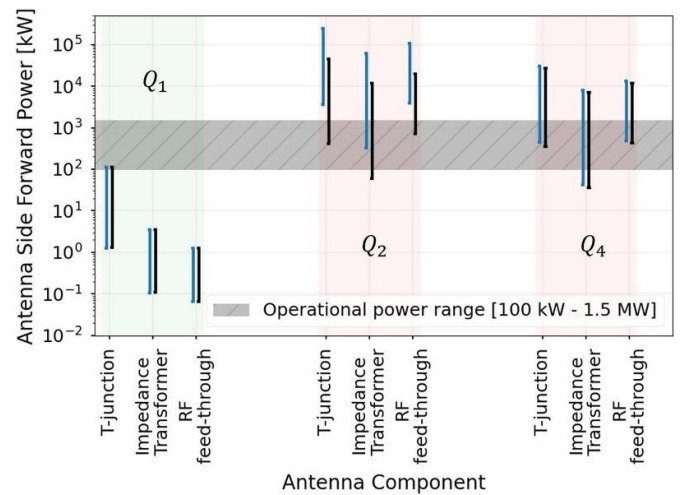


Figure 8. The forward powers of one generator triggering the multipactor in the T-junction, impedance transformer and RF feed-through of each antenna Q_1 , Q_2 , and Q_4 . The blue (respectively black) vertical lines correspond to the forward powers triggering multipactor in the components of the *left* (respectively *right*) side of each antenna. The grey hatched region corresponds to the nominal operational power range of one powered generator. Q_1 is powered (*tuned* capacitors), while Q_2 , and Q_4 are non-powered and their capacitors are *tuned* at 55 MHz. The non-conditioned TEEY data are used.

As an illustrative example, figure 9 represents the electric field cartography in the WEST ICRH antennas for a forward power of 1 MW for both generators of the antenna Q_1 . In this figure, the red arrows refer to the components where the multipactor is triggered.

Second, we have considered the *fully-conditioned* TEEY data curve (black curve of figure 5) for the silver-coated components and the conditioned TEEY data curve for the alumina ceramic (orange curve of figure 7). The results are illustrated in figure 10. There is no forward power range for which the multipactor is triggered in the RF feed-through component since there is no multipactor in this component for the conditioned TEEY data.

Figure 10 shows that the conditioning reduces the multipactor range in the various components of the WEST ICRH antennas and that within the [100 kW–1.5 MW] forward power range, there is almost no multipactor-trigger in the non-powered antennas when compared to the results of figure 8 except for the impedance transformer of Q_4 when the forward power is approximately equal to 1.5 MW.

4.2 Results-case 2

In this second case, both generators of the antenna Q_1 are powered with the same forward power, and the four capacitors are tuned for the antenna to resonate at 55 MHz. Q_2 and Q_4 are non-powered with their capacitors *detuned*. The results corresponding to the non-conditioned TEEY data curves are represented in figure 11. The latter shows that, due to the

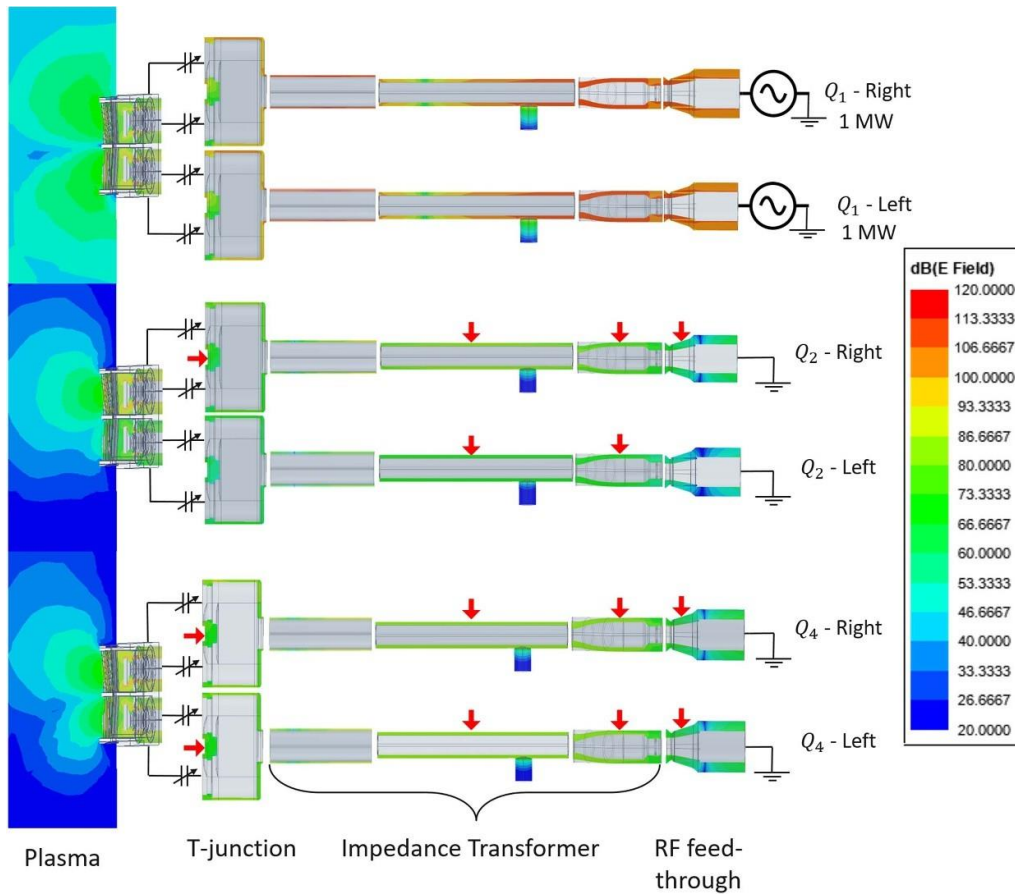


Figure 9. The electric field cartography in the various components of the three WEST ICRH antennas. Only Q_1 is powered with a forward power of 1 MW per antenna side. The components where the multipactor is triggered are indicated with red arrows.

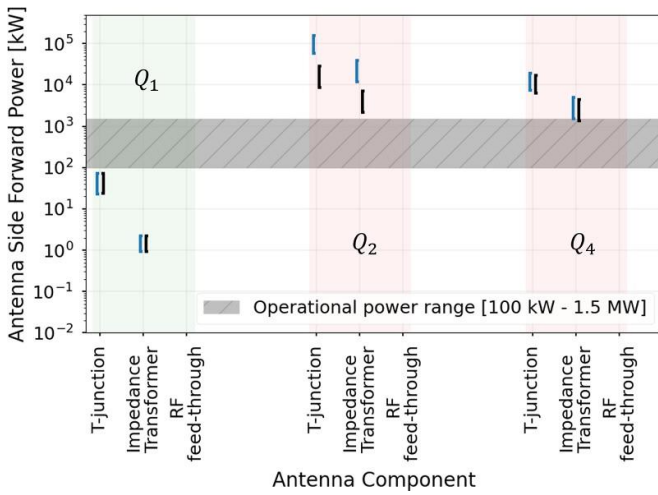


Figure 10. Same caption as figure 8. Q_1 is powered (*tuned* capacitors), while Q_2 , and Q_4 are non-powered and their capacitors are *tuned* at 55 MHz. The fully-conditioned TEEY data are used.

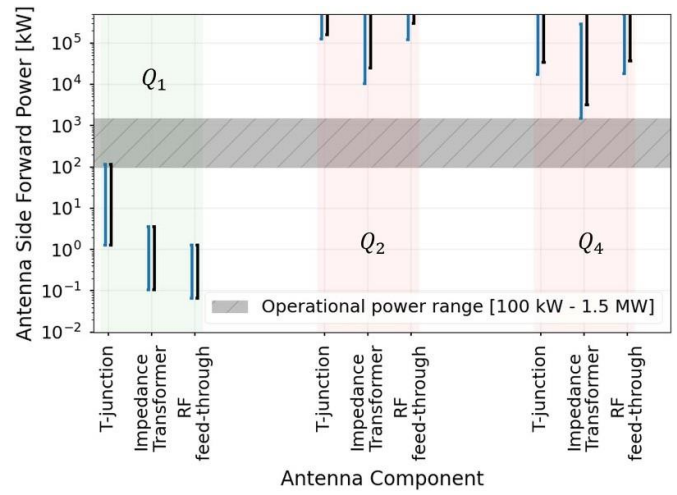


Figure 11. Same caption as figure 8. Q_1 is powered (*tuned* capacitors), while Q_2 , and Q_4 are non-powered and their capacitors are *detuned* at 55 MHz. The non-conditioned TEEY data are used.

capacitors detuning, there is almost no multipactor trigger in the non-powered antennas when compared to the results of figure 8 except for the impedance transformer of the Q_4 's

left side when the forward power is approximately equal to 1.5 MW. The multipactor is not triggered according to the conditioned TEEY data used.

5. Pressure rise formulation

In this section, we estimate the pressure rise caused by the multipactor avalanche whenever it takes place in the ICRH antennas' system of WEST. The estimated pressure rise will be compared to the one observed during the experiments on the tokamak WEST.

5.1. Problem formulation

We assume that the steady state is reached when a pressure rise is observed on an ICRH antenna since the time needed for the pressure to rise on the system is much greater than the rebounding time of the desorbed particles. Indeed, in such a case, it is possible to establish a balance equation between the rate of desorption and that of pumping.

Consequently, the molecular desorption balance equation is given by

$$+R - \phi \cdot S_p = 0 \quad (1)$$

where

- R is the surfaces' molecular desorbed rate (caused by multipactor) expressed in $[(\# \text{ molecules})/s]$.
- ϕ is the pump-impinging molecular flux defined as the number of molecules crossing a unit surface during a unit of time, and expressed in $[(\# \text{ molecules})/(\text{m}^2 \text{ s})]$.
- S_p is the pumping effective surface m^2 , depending on the pump system design.

R and ϕ are to be evaluated.

5.1.1. Pump-impinging molecular flux evaluation ϕ .

Knowing that the molecular distribution is spatially uniform and non-uniform in the velocity space, the molecular flux can be expressed as

$$\phi = \frac{1}{4} n \langle v \rangle \quad (2)$$

where, n is the molecular volume density expressed in $[(\# \text{ molecules})/\text{m}^3]$ and $\langle v \rangle$ is the gas molecules' mean speed expressed in ms^{-1} .

We assume that we are dealing with an ideal gas to evaluate the molecular volume density n given therefore by

$$n = \frac{N}{V} = \frac{p}{k_B T} \quad (3)$$

where N is the total number of molecules $[(\# \text{ molecules})]$, V is the gas volume m^3 , p is the gas pressure in $[\text{Pa}]$, k_B is the Boltzmann constant expressed in $[\text{JK}^{-1}]$, and T is the gas temperature in $[\text{K}]$.

The mean speed of gas molecules $\langle v \rangle$ $[\text{ms}^{-1}]$ is calculated by the Maxwell-Boltzmann distribution and is given by

$$\langle v \rangle = \frac{\sqrt{8k_B T}}{\pi m} \quad (4)$$

where, m is the mass of the desorbed molecules in $[\text{kg}]$.

5.1.2. Surfaces' molecular desorbed rate R . We rely on the X-ray photoelectron spectroscopy (XPS) [22, 23] data analysis, obtained for a WEST ICRH antenna representative material sample of silver-coated stainless steel, to monitor the chemical surface modifications [10], and relate it to the multipactor simulation results to estimate the molecular desorbed rate R .

The evaluation of R results from six steps summarized in the following:

- 1) Exploitation of the XPS data obtained after each *in-situ* conditioning phase to calculate the percentage of desorbed carbon atoms per electron dose. The evaluated quantity is denoted m_C and is expressed in $[\% \text{ Carbon}/\text{Cm}^{-2}]$.
- 2) Evaluation of the electron dose caused by the multipactor discharge. The latter is denoted d and is expressed in Cm^{-2} . The multipactor electron dose quantity is evaluated from the Spark-3D statistical data [11], giving the average multipactor electrons' impact density i expressed in em^{-2} . d is related to i through the elementary electron's charge $|q|$, where $d = i \times |q|$.
- 3) Evaluation of the desorbed carbon atoms' percentage caused by multipactor, obtained by multiplying the percentage of desorbed carbon atoms per electron dose m_C by the electron dose caused by the multipactor d . The quantity is denoted $p_C = m_C \times d$ and is expressed in $[\% \text{ Carbon}]$.
- 4) Calculation of the number of carbon $\# \text{ Carbons}_{S_{MP}}$ present on the surface contributing to the multipactor avalanche. The surface contributing to the multipactor is evaluated from Spark-3D, and is denoted as S_{MP} m^2 .
- 5) Calculation of the number of desorbed carbon due to multipactor:

$$\# \text{ desorbed}(\text{Carbon})_{S_{MP}} = \# \text{ Carbons}_{S_{MP}} \times p_C$$

- 6) Evaluation of the molecular desorbed rate:

$$R = \frac{\# \text{ desorbed}(\text{Carbon})_{S_{MP}}}{t}$$

where t is the time needed for the desorption to take place that we will consider equal to the multipactor simulation time—the time for the multipactor discharge to be sustained.

Now that the pump-impinging molecular flux ϕ and the molecular desorbed rate R are evaluated, we get back to the balance equation (equation (1)) and express the pressure rise (in $[\text{Pa}]$) caused by multipactor by the following:

$$p = \frac{R \sqrt{2\pi m k_B T}}{S_p} \quad (5)$$

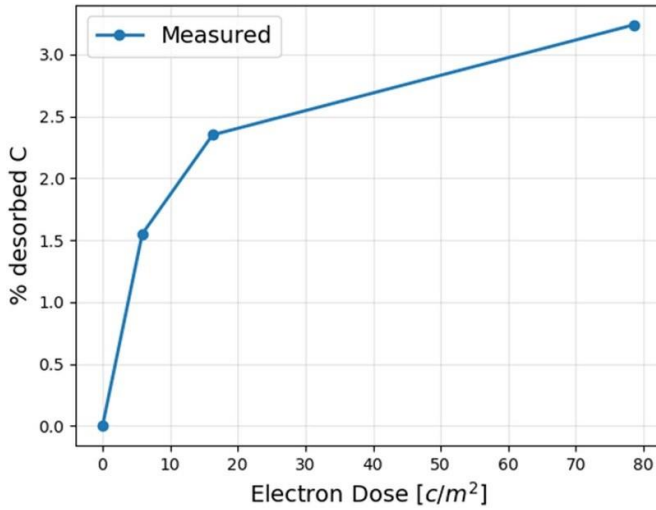


Figure 12. The percentage of desorbed carbon per cumulative electron dose received by the WEST ICRH representative sample.

52 Multipactor pressure rise estimation—numerical application

The WEST ICRH representative sample was subjected to the WEST operational conditions, where first, it was baked for three days at 200 °C to mimic the baking phase of the tokamak WEST. Then, it was conditioned by electron bombardment to eliminate the surface's impurities by desorbing the hydroxides, hydrocarbons, and contaminants from the sample surface while being maintained at a temperature of 70 °C—operational temperature of the antennas. The latter mimics the RF conditioning phase of the ICRH antennas before being used on plasma.

The XPS spectra, acquired at the different conditioning phases, showed the desorption—decrease in the concentration—of contaminants such as carbon and oxygen. We will be mainly interested in analyzing carbon desorption since it is the main desorbed species detected by XPS during electron bombardment. More details about the surface monitoring and the electron dose effect on the WEST ICRH representative sample are given in [10].

In particular, the percentage of desorbed carbon elements versus the cumulative electron dose received by the sample is given in figure 12, showing an increase in the carbon desorption with the electron dose.

As the volatile molecules are the most desorbed molecules during electron beam bombardment, we consider only the methane-based-desorbed molecules.

The estimation of m_C —the percentage of desorbed carbon atoms per electron dose—is done by linearly interpolating the first two percentages of desorbed carbon. We have chosen to linearly interpolating the first two data points as the electron dose estimated by the multipactor simulations lies within this range of values. Therefore

$$m_C = \frac{\Delta\%C}{\Delta\text{dose}} = 0.264. \quad (6)$$

The evaluation of the multipactor electrons' impact density (denoted i) relies on Spark-3D statistical simulations' outputs. In particular, we define the average electrons' impact density as the relevant quantity for the pressure rise evaluation. i should be estimated after the saturation of the multipactor phenomenon, i.e. the development of the electron cloud caused by the multipactor in the antennas' components. The latter is a limitation in Spark-3D⁵ since it does not account for any saturation mechanisms such as, for example, space charge effects. Nevertheless, if the simulation is forced for a long time, it could reach that time with a numerical plateau region in the number of electrons. Or even stops before, once the number of electrons reaches a maximum threshold—simulator internal parameter as the simulations are resource demanding.

For example, simulating the T-junction of the WEST ICRH antenna at 55 MHz for 10 000 ns, with the *non-conditioned* TEEY data curve leads to a numerical saturation in the number of electrons—a plateau region is observed. The average multipactor electrons' impact density evaluated in this case is $i = 1.284 \times 10^{14} \text{ em}^{-2}$. Consequently, the multipactor dose is $d = 2.05 \times 10^{-5} \text{ Cm}^{-2}$, and the desorbed carbon atoms' percentage is: $p_C = 0.5412 \times 10^{-5}\%$.

As we consider methane molecules, we can assume that one carbon atom exists per 10^{-20} m^2 . The number of carbon can be expressed as: $\#\text{Carbon}_{S_{MP}} = S_{MP} \times 10^{20}$, with S_{MP} corresponding to the T-junction component. Therefore, the number of desorbed carbon by the multipactor effect is $\#\text{desorbed}(\text{Carbon})_{S_{MP}} = 0.46 \times 10^{13}$. And the surfaces' molecular desorbed rate is $R = 4.6 \times 10^{17} [(\#\text{molecules})/\text{s}]$.

The pressure rise caused by the multipactor avalanche triggered in the T-junction of a WEST ICRH antenna is evaluated using equation (5), where the temperature is taken equal to the operational antenna temperature (70 °C) and m the methane molecule's mass. Accounting for methane fragments and methane molecules with oxygen elements, the methane mass is bounded by $1.67 \times 10^{-26} \text{ kg} \leq m \leq 8.34 \times 10^{-26} \text{ kg}$. Therefore, the pressure rise caused by the multipactor triggered in the T-junction geometry for the pumping effective surface of the WEST ICRH antennas is:

$$1.35 \text{ mPa} \leq p \leq 3 \text{ mPa}.$$

As the Spark-3D does not account for the space charge effects, we have conducted a simulation for a section of the impedance transformer—*Transition 2* defined in [11]—of the WEST ICRH antenna using a multipactor tool called SPIS that accounts for the space charge effects [24]. The simulation is performed at the frequency of 55 MHz for the *non-conditioned* TEEY data curve of the ICRH representative sample. It was found that the average current density of this geometry at the saturation level is 9 A m^{-2} . Consequently, the evaluated molecular desorbed rate for the region in question

⁵ Version 1.6.3.

is $R = 7.6 \times 10^{17} [(\# \text{molecules}) / \text{s}]$, and the pressure rise caused by the multipactor triggered in the impedance transformer is:

$$2.2 \text{ mPa} \leq p \leq 5 \text{ mPa}.$$

5 Discussion

At this step, we can compare the experimental pressure rise level to that caused by the multipactor phenomenon, as evaluated in section 5.2 by the developed steady-state formulation. Although the Spark-3D software does not model any saturation mechanism, there is a good agreement between the estimated pressure rise obtained via the multipactor simulations ($\sim 10^{-3}$ Pa) and the experimentally measured pressure rise (10^{-3} Pa– 10^{-2} Pa). This agreement is also evidenced when SPIS, a multipactor tool accounting for the space charge effects, is used. Therefore, the pressure rise observed on the ICRH antennas when only one antenna is active can be attributed to the multipactor phenomenon, as the pressure level caused solely by the multipactor phenomenon is within one order of magnitude of the experimentally measured pressure rise.

6 Conclusion

In this paper, we have investigated the problem causing the increase in the internal pressure level of the ICRH system of the tokamak WEST when only one antenna is powered. The findings indicate that when only one antenna of the WEST ICRH system is powered, while the remaining two are off, the multipactor is triggered in the various components—T-junction, impedance transformer, and RF feed-through—of the non-powered antennas due to the inter-antennas coupling. The latter indicates that the cause of the pressure rise can be explained by the multipactor when the *non-conditioned* WEST ICRH representative TEEY is used. Furthermore, the results show that the multipactor range is reduced when the *fully-conditioned* TEEY is used, and the capacitors of the off-mode antennas are detuned. Hence, detuning the capacitors of the non-powered antennas should be favorable when operating the antenna system. The latter finding agrees with the results obtained when we analyzed the multipactor occurrence during the RF conditioning phase of the WEST ICRH antennas [11]. From the other side, we have formulated the pressure rise problem and have found that the estimated pressure increase caused by the multipactor phenomenon is comparable to that experimentally measured. Consequently, the multipactor induced by the antennas' cross-talk is the most probable cause for the pressure rise observed internally in the non-powered antennas of the WEST ICRH system.

The main limitation of the present work is that we have not accounted for the toroidal magnetic field when estimating the lowest and highest multipactor electric field thresholds of each component of the WEST ICRH antenna, specifically that it is known that the DC magnetic field is responsible for altering the electrons' trajectories within the structures. Accounting for the effects of the DC field, which is inhomogeneous in the

radial direction inside the ICRH antenna, will be the purpose of future work.

ORCID iDs

Eva Al Hajj Sleiman  <https://orcid.org/0000-0003-2095-6870>

Julien Hillairet  <https://orcid.org/0000-0002-1073-6383>

Mohamed Belhaj  <https://orcid.org/0000-0001-6941-9932>

Vincent Maquet  <https://orcid.org/0000-0001-5539-3903>

References

- [1] Bucalossi J. *et al* 2022 Operating a full tungsten actively cooled tokamak: overview of WEST first phase of operation *Nucl. Fusion* **62** 042007
- [2] Hillairet J. *et al* (West Team) 2021 WEST actively cooled load resilient ion cyclotron resonance heating system results *Nucl. Fusion* **61** 096030
- [3] Delpech L. *et al* 2015 Evolution of the tore supra lower hybrid current drive system for WEST *Fusion Eng. Des.* **96–97** 452–7
- [4] Bernard J.-M. *et al* 2019 Commissioning of the first WEST load-resilient long pulse ICRF launcher in the TITAN testbed and on WEST plasmas *Fusion Eng. Des.* **146** 1778–81
- [5] Vaughan J. 1988 Multipactor *IEEE Trans. Electron Devices* **35** 1172–80
- [6] Graves T.P. 2006 Experimental investigation of electron multipactor discharges at very high frequency *PhD Thesis* Massachusetts Institute of Technology
- [7] Becerra G. 2007 Studies of coaxial multipactor in the presence of a magnetic field *PhD Thesis* Massachusetts Institute of Technology
- [8] Woo R. 1968 Multipacting discharges between coaxial electrodes *J. Appl. Phys.* **39** 1528–33
- [9] Woo R. 1970 Final report on RF voltage breakdown in coaxial transmission lines *Report* 32-1500 (National Aeronautics and Space Administration)
- [10] Al Hajj Sleiman E., Hillairet J., Belhaj M. and Dadouch S. 2022 Evaluation of multipactor thresholds for coaxial lines subject to surface conditioning for the west ion cyclotron antenna *Fusion Eng. Des.* **185** 113325
- [11] Al Hajj Sleiman E., Hillairet J. and Belhaj M. 2023 Multipactor-triggering powers' modelling of a west icrh antenna during RF conditioning *IEEE Trans. Plasma Sci.* **51** 1247–55
- [12] Graves T.P., Wukitch S.J., LaBombard B. and Hutchinson I.H. 2006 Effect of multipactor discharge on Alcator C-Mod ion cyclotron range of frequency heating *J. Vac. Sci. Technol. A* **24** 512–6
- [13] Goniche M., El Mhari C., Francisquez M., Anza S., Belo J., Hertout P. and Hillairet J. 2014 Modelling of power limit in RF antenna waveguides operated in the lower hybrid range of frequency *Nucl. Fusion* **54** 013003
- [14] Kim H., Verboncoeur J. and Lau Y. 2007 Modeling RF window breakdown: from vacuum multipactor to RF plasma *IEEE Trans. Dielectr. Electr. Insul.* **14** 774–82
- [15] Sorolla E. 2012 Contribution to modeling multipactor and corona discharges in high power electromagnetic fields *PhD Thesis* EPFL
- [16] Höhn F., Jacob W., Beckmann R. and Wilhelm R. 1997 The transition of a multipactor to a low-pressure gas discharge *Phys. Plasmas* **4** 940–4
- [17] Yu M. 2007 Power-handling capability for RF filters *IEEE Microwave Mag.* **8** 88–97

- [18] Helou W. *et al* 2015 Radio-frequency electrical design of the WEST long pulse and load-resilient ICRH launchers *Fusion Eng. Des.* **96–97** 473–6
- [19] Bosia G. 2003 High-power density ion cyclotron antennas for next step applications *Fusion Sci. Technol.* **43** 153–60
- [20] Bira S. 2021 Conception d'un résonateur quadripolaire pour la caractérisation des propriétés de couches minces supraconductrices en régime radiofréquence pour les cavités accélératrices *Theses* Université Paris-Saclay
- [21] Hillairet J. 2020 RF network analysis of the west ICRH antenna with the open-source python Scikit-RF package *AIP Conf. Proc.* **2254** 070010
- [22] Moulder J.F., Stickle W.F., Sobol W.M. and Bomben K.D. 1992 *Handbook of X-ray Photoelectron Spectroscopy* (Perkin-Elmer Corporation, Physical Electronics Division)
- [23] Hofmann S. *Auger- and X-ray Photoelectron Spectroscopy in Materials Science: A User-Oriented Guide (Springer Series in Surface Sciences vol 49)* (Springer)
- [24] Peysson Q., Belhaj M., Sarrailh P. and Payan D. 2022 New 3d simulation tool for multipactor in presence of dielectrics *Int. Workshop on Multipactor, Corona and Passive Intermodulation (MULCOPIM) (Valencia, Spain, 19–21 October 2022)*